ACS Sustainable Chemistry & Engineering

pubs.acs.org/journal/ascecg

Research Article

Efficient Electroreduction of High-Pressure Gaseous and Supercritical CO_2 to CO in a Zero-Gap Electrolyzer

Xiongwei Tian, Zheng Chen, Francesco Iacoviello, Mengyin Xie, Wenqing Chu, and Yuqun Zhuo*

Cite This: *ACS Sustainable Chem. Eng.* 2025, 13, 10495−10503

Read Online

ACCESS | Metrics & More | Article Recommendations | Supporting Information

ABSTRACT: The electroreduction of carbon dioxide (CO_2R) presents a promising avenue for mitigating CO_2 emissions while producing valuable chemicals. In this work, we report a novel pressure equilibrium strategy tailored for pressurized CO_2R in a zero-gap electrolyzer, aiming at accommodating the high-pressure CO_2 sources from its capture, utilization, and storage scheme. We investigated the impact of pressure on the CO_2R performance under both gaseous and supercritical conditions, while also examining the synergistic interplay of temperature with high pressure. Significant enhancement of energy efficiency (46.5%) with high CO Faradaic efficiency (94.4%) and low cell voltage (−2.72 V) was achieved at 200 mA/cm^2 under 75 bar and 80 °C. In addition, we noticed that the agglomeration and migration of salt precipitation within the gas diffusion electrode were effectively suppressed under pressurized conditions, which indicated the potential benefit for prolonged cell stability.

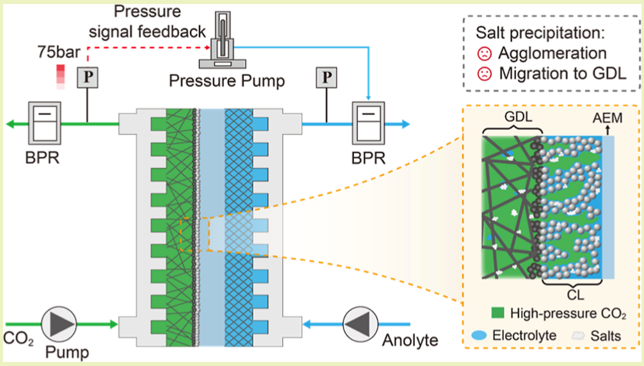

KEYWORDS: *CO_2 reduction, high-pressure, electrochemical engineering, pressure equilibrium, industrialization, salt precipitation*

1. INTRODUCTION

The electrochemical reduction of CO_2 (CO_2R) driven by renewable energies has led a promising pathway for closing artificial carbon cycle and producing valuable chemicals and fuels, including carbon monoxide (CO), formate/formic acid, alcohols, and hydrocarbons.[1−3] The research efforts in the past decade have primarily focused on elucidating the reaction mechanism and exploring new catalyst materials,[4−6] with comparatively less attention paid to other aspects such as the electrolyzer design or the optimization of experimental parameters (electrolyte composition, pressure, temperature, etc.), although these aspects hold the equal importance in determining the industrialization of CO_2R.[7−10]

The majority of studies to date have conducted CO_2R under ambient condition.[11,12] However, CO_2 is frequently pressurized as the effluent in various industrial processes such as natural gas reforming, soda ash production, and coal gasification.[13,14] Moreover, within the framework of carbon capture, utilization and storage (CCUS) scheme, CO_2 transported from capture points to the downstream utilization points, whether by vehicles, ships, or pipelines, must possess high-pressure conditions and often exist in supercritical state (∼100 bar).[15,16] Depressurizing these CO_2 sources to align with the existing ambient CO_2R equipment could inevitably compromise the energetic value of the reactants.[9,17]

The previous investigations of pressurized CO_2R are mainly conducted in aqueous batch cells.[18−20] Pressurization could significantly increase the solubility of CO_2 in an electrolyte and bring higher CO_2 coverage near the catalyst surface, thereby enhancing the current density, suppressing the hydrogen evolution reaction (HER) competition and regulating the CO_2R selectivity.[1,21] Notably, high formate selectivity could be obtained and even become catalyst independent with pressurized CO_2.[22] Some studies showed that circulating the electrolyte dissolved with pressurized CO_2 could enhance the current density to ∼100 mA/cm^2.[22−24] Theoretical modellings and control experiments were also performed to investigate CO_2R behavior under high-pressure conditions.[25−28] More recent findings suggested that pressurized CO_2 has facilitated C_{2+} product selectivity, such as acetate and ethanol.[29,30] Despite these advancements, most current studies on pressurized CO_2R were conducted under a fixed temperature. While it is established that elevated temperature tends to promote HER under ambient pressure conditions,[1] the impact of temperature under pressurized CO_2R remains largely unexplored. Therefore, systematic optimization of temperature

Received: March 13, 2025
Revised: June 18, 2025
Accepted: June 24, 2025
Published: June 28, 2025

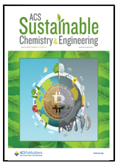

https://doi.org/10.1021/acssuschemeng.5c02275

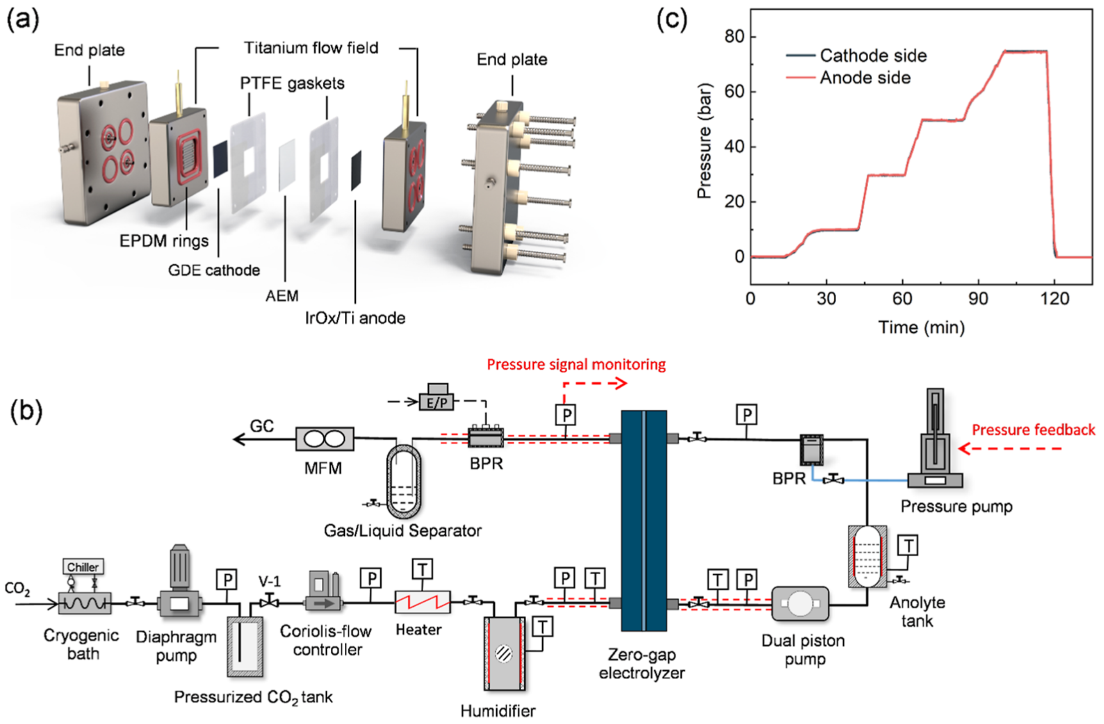

Figure 1. (a) Exploded view of the high-pressure zero-gap electrolyzer. (b) Schematic flowchart of the pressurized zero-gap electrolysis system. (c) The pressure profiles of the cathodic and anodic sides during a typical pressure increase/decrease process.

under pressurized environments is essential for improving CO_2R selectivity and efficiency.

The above results have shown the positive effects of pressurized CO_2R. However, the scalability of aqueous batch cells faces a challenge for industrial application.[31] To address this issue, a fuel-cell-like (zero-gap) electrolyzer has received much attention in recent years.[32,33] This configuration typically incorporates the gas diffusion electrode (GDE), directly feeding CO_2 through a porous carbon support to the catalyst, exhibiting both the feasibility for scale-up and the capability to meet the industrial reaction rate.[34,35] Moreover, different from merely enhancing CO_2 solubility in an aqueous electrolyte, elevating CO_2 pressure could directly increase its concentration at the triple-phase interface (the ionomer-coated catalyst/water/CO_2) inside the GDE, which may potentially regulate the local environment around the catalyst and influence the reaction pathways.[9,36,37]

Investigating the influence of the pressure on the CO_2R in zero-gap electrolyzers over a broad pressure range remains a significant technical challenge. The key obstacle is to establish a as minimal as possible pressure difference between the cathodic and anodic flow fields of the electrolyzer to ensure the normal function of the fragile cell components, such as membrane- and carbon-based GDE.[15,18] However, the density of CO_2 increases drastically during pressurization due to its low critical parameters (73.8 bar, 31 °C), experiencing a density change of more than 2 orders of magnitude from the gas state to the supercritical state (Figure S1). The quick density change may lead to pressure fluctuations within the cathodic flow channel, posing a substantial challenge for pressure equilibrium control between two sides of the zero-gap electrolyzer.[38,39] Moreover, the structure and assembling torque of the electrolyzer should be carefully optimized to ensure effective cell sealing under high pressure while maintaining appropriate compression of the GDE.[39] To our knowledge, due to the difficulties mentioned above, the reported studies of pressurized CO_2R in typical zero-gap electrolyzers have been limited below 10 bar.[40,41]

Herein, we propose a novel pressure equilibrium strategy tailored for pressurized CO_2R in a custom-built zero-gap electrolysis system. The impact of pressure on the CO_2R is investigated across both the CO_2 gaseous and supercritical states, increasing the pressures up to 75 bar. The synergistic effect of temperature is also explored with pressure. Furthermore, the pressure influence on the salt precipitates distribution within the GDE is evaluated.

2. EXPERIMENTAL SECTION

2.1. Materials. All chemical reagents were purchased from commercial suppliers (Sigma-Aldrich and Aladdin) and were at least of analytical grade. They were used without further purification. Milli-Q grade (ρ = 18.2 MΩ cm) ultrapure deionized (DI) water was used to prepare all of the solutions.

2.2. Electrode Preparation. To prepare the cathode GDE, silver (Ag) nanoparticles (d_{avg} < 150 nm, Sigma-Aldrich) were dispersed in isopropanol at a concentration of 5 mg/mL, together mixed with a 5 wt % PiperION A5 ionomer solution. The ink solution was homogenized in an ultrasonic bath for 20 min with the bath temperature being carefully maintained below 30 °C by ice chunks. Then, the Ag dispersion was sprayed onto a Sigracet 39 BB carbon gas diffusion layer (GDL) using a hand-held airbrush with N_2 as the carrier gas. The cathode catalyst loading was 1.0 ± 0.1 mg/cm^2. The IrO_x-sintered porous titanium frit (0.25 mm thick) with a mass loading of 1.0 ± 0.1 mg/cm^2 was used as an anode.

The commercially available PiperION A40-HCO_3 anion exchange membrane (AEM) was employed in all of the tests. The membrane was activated by immersing in 1 M KOH solution for 24 h, during which the solution was changed to fresh after the first 5 h. The membrane was flushed with ample ultrapure DI water before being used and then mounted to the zero-gap electrolyzer in its hydrated state.

2.3. Electrode Characterization. All of the tested GDE samples in this work were carefully stored for characterization in a vacuum oven at room temperature immediately after dissembling the electrolyzer to prevent any possible contamination or reaction with ambient CO_2. The field emission scanning electron microscopy (SEM) images were obtained by using a JSM-IT800 (JEOL, Japan) equipped with an energy-dispersive X-ray (EDX) spectroscopy detector to examine the morphology and elemental distribution of the electrodes. The microscope was operated at 8 kV acceleration voltage. X-ray diffraction (XRD) patterns were gained on a SmartLab X-ray diffractometer (Rigaku, Japan) equipped with the Cu Kα radiation source. The X-ray photoelectron (XPS) spectrum was performed on an ESCALAB 250Xi spectrometer (Thermo Fisher, USA) using the Al Kα radiation exciting source. Survey scans were acquired in a binding energy range of 0−1361 eV with an analyzer pass energy of 100 eV. An EasyDrop type instrument (Krüss, Germany) was used to measure the water wetting properties (e.g., contact angles) of the GDE before and after the experiments under different pressure conditions. A drop of water was formed on the GDE plate with a syringe, and the drop contours captured by the CCD camera of the goniometer were analyzed.

The content of potassium cations (K^+) within the GDE was measured with inductively coupled plasma mass spectrometry (ICP−MS, Agilent 7900, USA). To collect K^+ from the GDE, the GDE sample was fully dissolved in 15 mL of 10% v/v HNO_3 (Sinopharm Chemical Reagent Co., Ltd.), sealed in a centrifuge tube, and then ultrasonicated in an ice bath sonicator for 30 min. The resulting liquid sample was filtered through a 0.45 μm needle filter and diluted 10 folds with deionized water for analysis. The ICP−MS calibration was performed with a 5-point calibration curve obtained from the standard K^+ reagent (Guobiao (Beijing) Testing & Certification Co., Ltd.). Sc and ^{6}Li were used as the internal standards.

X-ray tomographic image acquisition of the GDE was performed using X-ray microcomputed tomography (Micro-CT, ZEISS Xradia 620 Versa, Carl Zeiss Inc., CA, USA). All samples were scanned with a source voltage of 100 kV and an exposure time of 2 s per projection, acquiring 2001 projections per scan. The raw transmission images from the scan were reconstructed using a commercial image reconstruction package (Reconstructor Scout-and-Scan, Carl Zeiss Inc., CA, USA), which uses a cone-beam-filtered back-projection algorithm, resulting in an isotropic voxel volume of approximately 480 nm.

2.4. High-Pressure Zero-Gap Electrolyzer. A custom-designed zero-gap electrolyzer, featuring a 1.5 × 1.5 cm^2 active area, has been employed for pressurized CO_2R measurements (Figure 1a). The anode and cathode end plates and flow fields are made of high-quality titanium. A fresh PiperION A40-HCO_3 membrane (3 × 3 cm^2) is intercalated between the anode and cathode. To secure the electrodes in position and regulate the compression of the GDE, two 0.24 mm PTFE gaskets are mounted surrounding the electrodes. Cell sealing is achieved by incorporating two symmetrical layers of ethylene−propylene−diene monomer (EPDM) rings in each flow field plate, wherein the inner EPMD rings are directly pressed against the membrane periphery. The cell is assembled using eight M6 bolt screws, each gradually tightened to a torque of 10 N m. This specific torque value is designed to guarantee the optimal contact between the GDE and the membrane, concurrently ensuring effective cell sealing during high-pressure tests. The temperature of the electrolyzer is regulated by two cartridge heaters horizontally inserted into each end plate and connected to an external temperature controller, with feedback from two thermocouples imbedded into the vertical position of the end plates. The photographs of the zero-gap electrolyzer are shown in Figure S4.

2.5. Electrochemical Measurements. All measurements were performed in a two-electrode setup using a Gamry Reference 3000 Electrochemical Station (Gamry, USA) at the galvanostatic mode. No IR correction was applied to the voltage values throughout the manuscript. The electrochemical impedance spectra have been conducted at open-circuit potential with 10 mV RMS perturbation in the frequency range from 100 kHz down to 1 Hz, with 10 points per frequency decade, and then the cell resistance could be determined by the high-frequency intercept with the real axis of the Nyquist plot. Linear sweep voltammetry (LSV) curves were recorded at a scan rate of −10 mV/s from 0 V to −3.2 V.

2.6. Product Analysis. The composition of gas products was analyzed using a gas chromatograph (Agilent 990 micro-GC, USA) equipped with a thermal conductivity detector. Two Molsieve 5 Å columns in separate channels were utilized for the separation of H_2 and CO, employing helium and argon as the carrier gas, respectively. The volumetric ratio of gas products was derived from the output peak areas based on the external standard curves. The cathode outlet stream was collected by using gas sampling bags for detection.

3. RESULTS AND DISCUSSION

3.1. Pressure Equilibrium Strategy for a Zero-Gap Electrolysis System. To achieve pressure equilibrium of the cathodic and anodic sides of the electrolyzer, we design a pressure monitoring and automatic tracking strategy for the pressurized zero-gap electrolysis system. As depicted in Figure 1b, a high-precision Back Pressure Regulator (BPR) is integrated at the cathodic outlet, enabling a precise control of CO_2 pressure at both gaseous and supercritical states. The pressure at the cathodic outlet is monitored by a highly sensitive pressure transducer positioned before the BPR, and the signal is real-time transmitted to a Pressure Pump (PP), allowing for prompt and automated control of the BPR opening at the anodic outlet in response to the detected cathodic pressure changes. Furthermore, considering the disparity of pressurizing behaviors of CO_2 and anolyte streams, a compensation value is set inside the program of PP to accurately adjust the pressure difference between two sides of the electrolyzer. This strategy allows a precise control of the system pressure by merely adjusting the cathodic BPR's parameter and the PP's compensation value. Further elucidation of the pressurized zero-gap electrolysis system and comparison of different pressure equilibrium strategies considered in this work are provided in Supporting Information Notes 1 and 2.

The pressure profile at the two sides of the electrolyzer in a typical pressure increase/decrease process is shown in Figure 1c. The system pressure stayed at different plateaus for electrochemical tests and reached a maximum value of 75 bar. It is evident that the pressure at the anode side consistently followed the pressure at the cathode side, and the pressure difference between two sides could be well controlled below 3 bar (Figure S5). The photographs of the GDE and AEM before and after the pressurized tests revealed that both components maintained their normal status throughout the testing (Figure S6). Moreover, the water contact angle has been measured for both the catalyst and gas diffusion sides of the GDE before and after different pressurized CO_2R experiments (Figure S7), and the minimal variations indicated that the hydrophobic characteristics of the GDE were unaffected after the high-pressure electrolysis.

3.2. Pressure Effect on CO_2R Performance. The pressurized electrolysis tests were conducted at 1, 10, 30, 50, and 75 bar, respectively. It might be necessary to point out that CO_2 at 75 bar (T = 60 °C) already reaches supercritical state, exhibiting low viscosity, high diffusivity like a gas, but with high density close to liquid (Table S1).[42] Supercritical CO_2 could expand to fill the whole containing space and is fully miscible with gas in any proportion.[43] The presence of supercritical CO_2 can be confirmed by the characteristic disappearance of

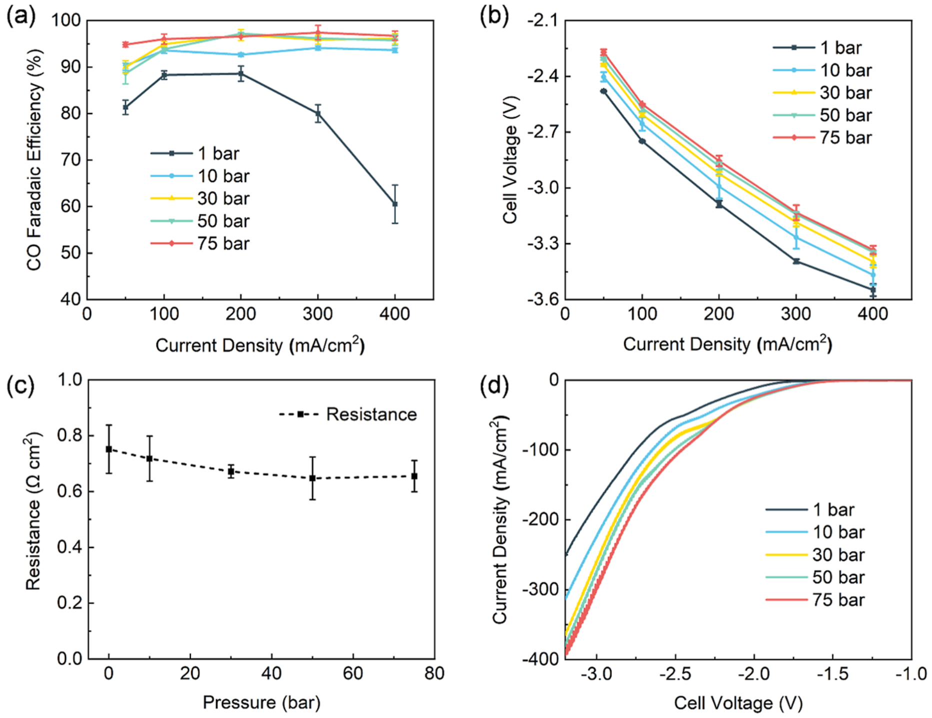

Figure 2. Effect of pressure on (a) FE_{CO} and (b) cell voltage under various current densities. (c) Cell resistance and (d) LSV curves at different pressures. The inset of (c) shows the pressure influence on cell resistance. All tests were operated with a 0.1 M KOH anolyte at $T = 60$ °C.

the $CO_2(l)/CO_2(g)$ interface within the cavity of the humidifier (Figure S8).

As illustrated in Figure 2a, pressurized CO_2 could prominently enhance the CO selectivity (denoted as FE_{CO}). At ambient pressure (1 bar), FE_{CO} rapidly decayed to 60.5% as the current density increased to 400 mA/cm^2. However, this issue could be effectively solved by elevating the CO_2 pressure. Specifically, at 10 bar, FE_{CO} surpassed 90% at all of the tested current densities. The maximum FE_{CO} of 96.7% was achieved at 75 bar at 400 mA/cm^2. This increase of CO selectivity under high pressure conditions agrees with previous reports.[17,40] Given the cumulative FE of CO and H_2 approaching 100% (Figure S9), the formation of other products at high-pressure tests could be negligible.

The enhancement of CO selectivity under pressurized conditions could be comprehended from multiple aspects: (i) the denser CO_2 at high pressure facilitates the diffusion-dominated mass transfer within the micropores of the GDE, contributing to higher CO_2 surface coverage at catalyst active sites;[44] (ii) the increased CO_2 concentration under pressurized conditions could modulate the microenvironment of the catalyst surface to be less basic, which is beneficial for CO selectivity, as demonstrated by a recent modeling simulation;[45] and (iii) the amount of water vapor carried by the humidified CO_2 stream under high pressure is significantly decreased as discussed in Supporting Information Notes 3 and 4, which could substantially alter the CO_2/water ratio at the three-phase interface, inhibiting HER competition and promoting CO_2R performance.[46,47] Moreover, the CO_2 volumetric flow rate decreases with increasing pressure, and thus the residence time of CO_2 increases within the cathodic flow fields. The extended residence time might also benefit the CO selectivity. However, the comparison of test results from different volumetric flow rates at 30 bar indicated that this influence could be neglected (Figure S11).

A decrease of approximately 200−250 mV in cell voltage could be observed from 1 to 75 bar under different current densities (Figure 2b). The cell resistance in different cell assemblies demonstrated a decrease of approximately 0.11 Ω cm^2 from 1 to 75 bar (Figure 2c), which can be attributed to the enhanced compactness of the sandwich structure of electrodes and membrane under elevated pressure. However, this decrease of ohmic voltage loss did not entirely account for the whole cell voltage drop. Given that the elevated pressure was not expected to bring electrochemical benefit for the anodic oxygen evolution reaction, we speculated that the CO_2 reactivity could be promoted through elevating CO_2 pressure.[17] This was supported by the positive shift of the onset potential on the LSV curves with increasing pressure (Figure 2d), suggesting a thermodynamic favor for pressurized CO_2R.

It should be noted that the pressure benefits to both FE_{CO} and cell voltage plateaued around 30 bar, suggesting only minimal improvement with a further pressure increase. Additionally, the current study did not show the influence of CO_2 phase shift from gaseous to supercritical on CO_2R performance, unlike the previous reports with supercritical CO_2R in single-compartment electrolyzers.[18,48] This could be attributed to the fact that alkaline CO_2R with a commercial silver catalyst has already achieved a decent CO selectivity under ambient conditions, which leaves little space for further improvement. Therefore, future research may need to focus on CO_2R schemes suffering from poor CO_2R efficiencies, such as acidic-fed electrolysis or the production of C_{2+} chemicals.[49,50] Moreover, integrating pressure regulation with other strategies, such as catalyst design or electrolyte engineering, could provide a complementary approach to further improve the CO_2R performance.[51]

The CO_2 crossover is a common issue in CO_2R with AEM systems. During electrolysis, excess CO_2 reacts with electro-

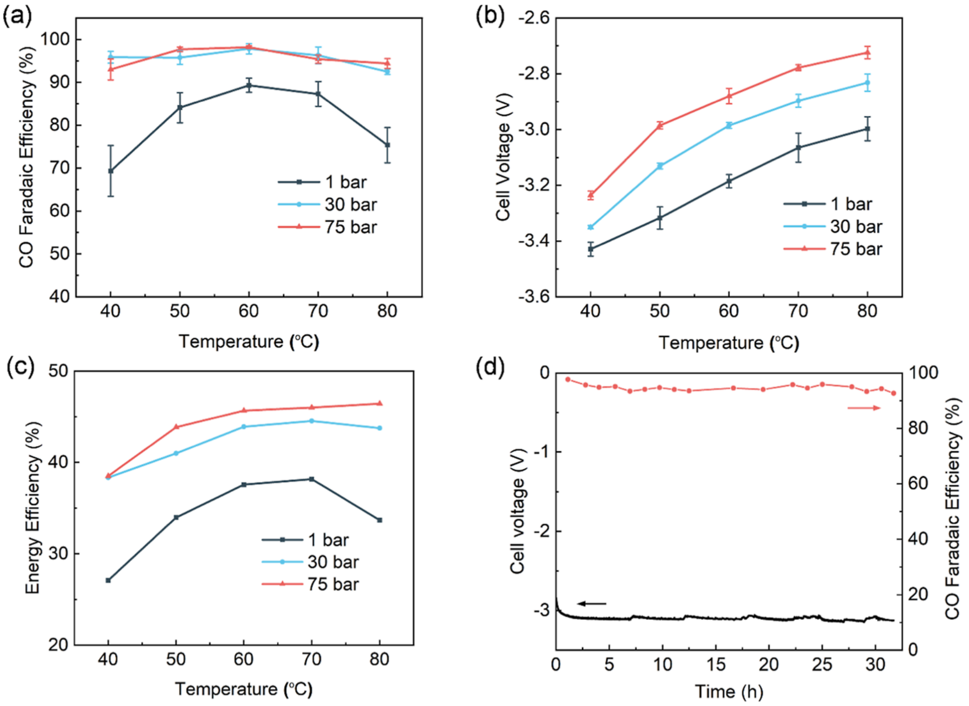

Figure 3. Effect of temperature on (a) FE_{CO}, (b) cell voltage, and (c) energy efficiency at 1 bar, 30 bar, and 75 bar. All tests were operated with a 0.1 M KOH anolyte at 200 mA/cm^2. (d) Stability test of pressurized CO_2R at 200 mA/cm^2 with pressure and temperature being set to 75 bar and 60 °C, respectively. The 0.1 M KOH anolyte was replenished every 5−6 h.

generated OH^-, forming (bi)carbonates, which diffuse through AEM as the charge carrier to form the inner electric circuit and finally be released with the anode gas.[7] The crossover of CO_2 would decrease CO_2 utilization efficiency. We evaluate the pressure dependency of CO_2 crossover in this work. As discussed in Supporting Information Note 5 and Figure S13, the CO_2 content in the anode gas was approximately 66.7%, indicating that CO_3^{2-} serves as the primary charge carrier at ambient pressure. This observation aligns with the findings of Janákey's group, who employed a similar zero-gap setup with PiperION membranes.[7] As the pressure increased, the CO_2 composition gradually rose to around 80%, suggesting a transition toward HCO_3^- as the dominant charge carrier. This trend is reasonable as elevated pressure increases the CO_2 concentration at the cathode−membrane interface, facilitating HCO_3^- formation. These results demonstrate a clear pressure dependence of CO_2 crossover in the zero-gap electrolyzer. However, an electrochemical stoichiometric limit of approximately 80% CO_2 crossover constrains the extent of this effect.

3.3. Temperature Effect on CO_2R Performance.

Temperature is another important parameter that affects the reactive performance. In this study, we evaluated the temperature effect on CO_2R at 1 bar, 30 and 75 bar, with temperature varying from 40 to 80 °C. The accuracy of the reactor's temperature regulation is confirmed in Table S6. As shown in Figure 3a, at ambient pressure, FE_{CO} initially increased with raising temperature but exhibited a significant decline after 60 °C. This decrease of FE_{CO} at high temperature aligns with prior reports as the competitive HER kinetics is preferred at high temperature.[1,40] However, FE_{CO} could be maintained at approximately 95% even at 80 °C under pressurized conditions. This resilience at high temperature could also be attributed to the higher concentration of local CO_2 near the catalyst and the reduced supplement of water vapor (less possibility for HER) under high pressure.

The cell voltage also benefited from the elevated temperature (Figure 3b). An obvious decrease of ~500 mV in cell voltage could be observed from 40 to 80 °C at both 30 and 75 bar. The notable voltage decrease, coupled with the well-maintained CO selectivity, have substantially promoted the operating efficiency of the zero-gap cell. As demonstrated in Figure 3c, the energy efficiency was improved from 27.1% (40 °C, 1 bar) to 46.5% (80 °C, 75 bar) at 200 mA/cm^2, underscoring a synergistic positive influence of elevated pressure and temperature on reducing the electrical energy consumption for the CO_2R.

The superior CO selectivity and low cell voltage suggest a powerful motivation for conducting the CO_2R under high-pressure and high-temperature conditions. However, it is essential to recognize that excessively high operating temperature may lead to the degradation of membrane performance, such as increased resistance, deteriorated ion-conduction, or cracking.[52,53] Since the recommended highest operating temperature for the PiperION membrane is 90 °C, it is advisable to set the operating temperature at 60−70 °C to ensure the membrane performance. A stability test has been performed over 32 h with the cell pressure and temperature being set to 75 bar and 60 °C, respectively (Figure 3d). The marginal change in cell voltage and CO selectivity throughout the test confirmed the stability of the system under pressurized conditions. This finding also provides valuable insights to develop CO_2R schemes with high-temperature-resistant membranes to further harness the pressure and temperature coupling benefits. Furthermore, we summarized the key testing parameters for pressurized CO_2R from recent studies in Table S8. As demonstrated, the pressure equilibrium strategy proposed allows for the systematic investigation of pressure

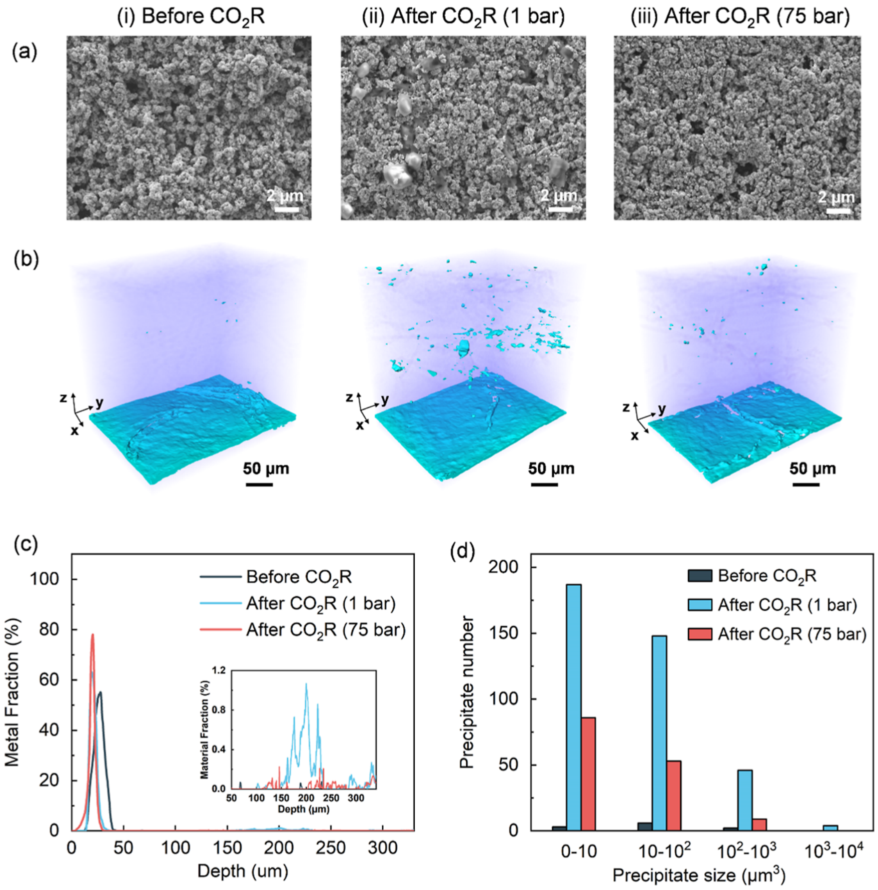

Figure 4. (a) SEM images of the catalyst layer (CL) before and after CO$_2$R at 1 and 75 bar. (b) Micro-CT 3D reconstruction of the GDE before and after CO$_2$R tests at 1 and 75 bar, with only metal (Ag or K) and pore materials displayed for clearly visualizing the precipitate distribution within the GDL. (c) Metal (Ag or K) fraction along the cross-direction of the GDE, with the inset highlighting the precipitate formation within the GDL. (d) Histogram of the precipitate size distribution within the GDL (depth in 50−340 μm). All tests were operated with a 0.1 M KOH anolyte at 200 mA/cm^2 for 2 h. The temperature was set to 60 °C.

effects on the CO$_2$R in zero-gap electrolyzers across a wider pressure range than previously achieved. Additionally, we performed the longest stability test for pressurized CO$_2$R reported to date, underscoring the robustness of our system.

3.4. Salt Precipitation in the GDE under Pressurized CO$_2$R Tests. The formation of salt precipitates inside the GDE is a common difficulty troubling the stable operation of zero-gap electrolyzers with an alkaline anolyte. These precipitates arise from the unintended alkaline cation crossover from the anolyte to cathode, where it reacts with CO$_2$ and the electrogenerated OH$^-$.[32] The precipitates could block the catalyst-active sites and gas transport microchannels and consequently deteriorate the electrolysis performance.[54] Considering a denser CO$_2$ environment under high pressure, it is imperative to pay extra attention to salt precipitation in our study.

SEM and EDX mapping were employed to examine the salt precipitate distribution in GDEs under both ambient and pressurized conditions. As shown in Figure 4a, the catalyst surface and pores were occupied by the salts after the test at 1 bar, which were further identified as potassium precipitates by EDX mapping (Figure S14b). Interestingly, no obvious salts could be observed on the catalyst surface for the GDE tested at 75 bar. We also noticed that the salts became gradually less observable on the catalyst surface as the pressure increased from atmospheric to 75 bar, with the appearance of the salts changing to isolated small crystals for the GDEs tested at high-pressure conditions (Supporting Information Note 4). ICP−MS analysis was used to measure the quantity of potassium within the GDE (Figure S19), and the result demonstrated that the potassium content remained at the same magnitude, showing no obvious variation at different pressures. Therefore, we assume that the salt content remains roughly consistent within the GDE under different pressure conditions, but the morphological appearance and distribution of the salts might be altered under high-pressure conditions.

Recognizing that SEM−EDX analysis provides only surface information on the GDE, X-ray microcomputed tomography (micro-CT) and material segmentation technique were utilized to explore the three-dimensional distribution of salts inside the GDE (Supporting Information Note 5). The metal component within the GDL of the GDE is mainly potassium precipitates for the tested GDE samples. As shown in Figure 4b,c, apparently fewer potassium precipitates could be observed within the GDL tested at 75 bar than those tested at 1 bar. Statistical analysis of the precipitate volume within the GDL reveals that the precipitate content at 1 bar exceeds that at 75 bar by a factor of 6.67. Additionally, the maximum size of precipitates formed at 1 bar is 8087 μm^3, which is approximately 1 order of magnitude larger than that formed at 75 bar (Figure 4d and Table S3).

The substantial difference in salt precipitation behaviors under ambient and pressurized conditions may seem counter-intuitive. To elucidate this disparity, it is important to understand that the salt precipitation process typically involves three stages: dissolved salt transfer, saturated salt nucleation, and crystal growth.[55] Additionally, the continuous solution film is essential for the continued salt crystal growth and agglomeration, acting as a bridge for salt transport.[56] Under high-pressure conditions, the dense gaseous/supercritical CO_2 has limited solubility in water and might lead to a biphasic system, featuring gaseous/supercritical CO_2 clusters and discretely distributed salt solution within the porous medium, which has been widely studied in CO_2 geological sequestration fields.[57,58] We assume that a similar scenario occurs within the pores of the CL, where pressurized CO_2 permeates the major spaces within the CL. The nonpolar CO_2 serves as an inert medium, exhibits poor salt solubility, and thus hinders the solute transportation (Figure 5a,b).[55,56] Consequently, the agglomeration of salt precipitates in the CL could be effectively suppressed, in which only isolated single potassium crystals could be formed under high-pressure conditions. A similar effect on agglomeration suppression of the nanoparticle catalyst was also reported in a previous supercritical CO_2 electrolysis study.[18]

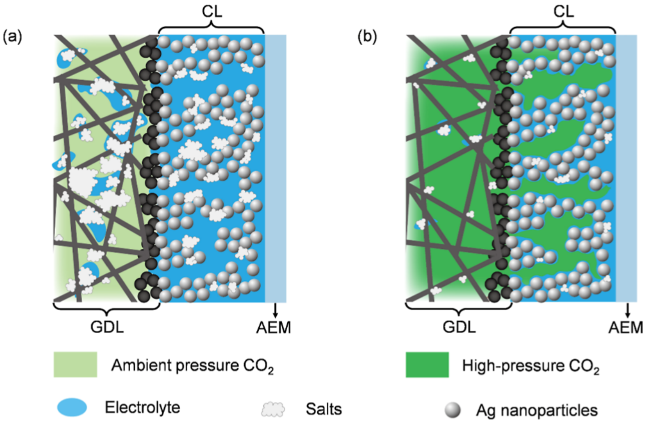

Figure 5. Schematic illustration of salt precipitation inside the GDE during CO_2R tests. (a) Electrolyte-filled CL pores and floods into the GDL, favoring the precipitate formation under ambient pressure. (b) Dense CO_2 occupies the pores of GDL and CL, suppressing the agglomeration and migration of salt precipitates under high-pressure conditions.

Regarding the significantly reduced distribution of salts within the GDL, the recent operando wide-angle X-ray scattering studies by Seger's group indicated that the movement of salt precipitates into the GDL could be correlated with electrolyte flooding via dissolution−precipitation cycles.[59,60] However, the dense CO_2 filling into the space of the GDL in the high-pressure scheme might create a steric barrier to electrolyte flooding, which could effectively restrain the migration of salt precipitates to the GDL.[55,61] Therefore, we conclude that both the agglomeration and migration of salt precipitation within the GDE are suppressed under high-pressure conditions, which could potentially strengthen the stability of CO_2R in zero-gap electrolyzers.

4. CONCLUSION

In summary, within the broader framework of CCUS, we have proposed and implemented a novel pressure equilibrium strategy for pressurized CO_2R in a zero-gap electrolyzer. The setup has demonstrated the capability to maintain a stable operation of critical cell components at pressures up to 75 bar. The elevated cell pressure and temperature have synergistically ensured the high CO selectivity and lower cell voltage and thus extensively improved the system energy efficiency. Notably, the pressurized condition brings forward an unforeseen benefit of suppressing the agglomeration and migration of salt precipitation within the GDE, suggesting a possible direction for extending cell stability through high-pressure operation.

■ ASSOCIATED CONTENT

Supporting Information

The Supporting Information is available free of charge at https://pubs.acs.org/doi/10.1021/acssuschemeng.5c02275.

> CO_2 phase diagram and density variation with pressure, discussion of different pressure equilibrium strategies, introduction of the pressurized zero-gap electrolysis system, energy efficiency figure, stability test result, calculation of water vapor amount carried by CO_2, SEM−EDX and Micro-CT images of the GDE, ICP−MS measurement of potassium within the GDE, and XRD and XPS spectrum of the Ag catalyst at different conditions (PDF)

■ AUTHOR INFORMATION

Corresponding Author

Yuqun Zhuo − *Key Laboratory of Thermal Science and Power Engineering of the Ministry of Education, Department of Energy and Power Engineering, Tsinghua University, Beijing 100084, China; Shanxi Research Institute for Clean Energy, Tsinghua University, Taiyuan 030000, China;* orcid.org/0000-0002-8407-4976; Email: zhuoyq@tsinghua.edu.cn

Authors

Xiongwei Tian − *Key Laboratory of Thermal Science and Power Engineering of the Ministry of Education, Department of Energy and Power Engineering, Tsinghua University, Beijing 100084, China;* orcid.org/0009-0008-8065-7104

Zheng Chen − *Key Laboratory of Thermal Science and Power Engineering of the Ministry of Education, Department of Energy and Power Engineering, Tsinghua University, Beijing 100084, China*

Francesco Iacoviello − *Electrochemical Innovation Lab, Department of Chemical Engineering, University College London, London WC1E 7JE, U.K.;* orcid.org/0000-0003-3564-2380

Mengyin Xie − *Key Laboratory of Thermal Science and Power Engineering of the Ministry of Education, Department of Energy and Power Engineering, Tsinghua University, Beijing 100084, China*

Wenqing Chu − *Key Laboratory of Thermal Science and Power Engineering of the Ministry of Education, Department of Energy and Power Engineering, Tsinghua University, Beijing 100084, China*

Complete contact information is available at: https://pubs.acs.org/10.1021/acssuschemeng.5c02275

Notes

The authors declare no competing financial interest.

ACKNOWLEDGMENTS

This project was supported by the Tsinghua University Initiative Scientific Research Program (No. 20213080036). The authors extend our gratitude to Linlin Xu for her assistance with Micro-CT tests and process. Additionally, the authors acknowledge Prof. Qi Lu and Donghuan Wu for insightful suggestions in zero-gap electrolyzer assembling and testing.

REFERENCES

(1) Kibria, M. G.; Edwards, J. P.; Gabardo, C. M.; Dinh, C. T.; Seifitokaldani, A.; Sinton, D.; Sargent, E. H. Electrochemical CO_2 Reduction into Chemical Feedstocks: From Mechanistic Electrocatalysis Models to System Design. *Adv. Mater.* **2019**, *31* (31), No. e1807166.

(2) Chen, J.; Wang, L. Effects of the Catalyst Dynamic Changes and Influence of the Reaction Environment on the Performance of Electrochemical CO_2 Reduction. *Adv. Mater.* **2022**, *34* (25), No. e2103900.

(3) Farooqi, S. A.; Farooqi, A. S.; Sajjad, S.; Yan, C.; Victor, A. B. Electrochemical Reduction of Carbon Dioxide into Valuable Chemicals: A Review. *Environ. Chem. Lett.* **2023**, *21* (3), 1515−1553.

(4) Gao, D.; Arán-Ais, R. M.; Jeon, H. S.; Roldan Cuenya, B. Rational Catalyst and Electrolyte Design for CO_2 Electroreduction towards Multicarbon Products. *Nat. Catal.* **2019**, *2* (3), 198−210.

(5) Zhang, X.; Zhou, Z. Perspective on Theoretical Models for CO_2 Electrochemical Reduction. *J. Phys. Chem. C* **2022**, *126* (8), 3820−3829.

(6) Xu, A.; Govindarajan, N.; Kastlunger, G.; Vijay, S.; Chan, K. Theories for Electrolyte Effects in CO $_2$ Electroreduction. *Acc. Chem. Res.* **2022**, *55* (4), 495−503.

(7) Endrődi, B.; Samu, A.; Kecsenovity, E.; Halmágyi, T.; Sebők, D.; Janáky, C. Operando Cathode Activation with Alkali Metal Cations for High Current Density Operation of Water-Fed Zero-Gap Carbon Dioxide Electrolyzers. *Nat. Energy* **2021**, *6* (4), 439−448.

(8) Xie, K.; Ozden, A.; Miao, R. K.; Li, Y.; Sinton, D.; Sargent, E. H. Eliminating the Need for Anodic Gas Separation in CO_2 Electroreduction Systems via Liquid-to-Liquid Anodic Upgrading. *Nat. Commun.* **2022**, *13* (1), 3070.

(9) Gabardo, C. M.; Seifitokaldani, A.; Edwards, J. P.; Dinh, C.-T.; Burdyny, T.; Kibria, M. G.; O'Brien, C. P.; Sargent, E. H.; Sinton, D. Combined High Alkalinity and Pressurization Enable Efficient CO2 Electroreduction to CO. *Energy Environ. Sci.* **2018**, *11* (9), 2531−2539.

(10) Ahn, S. T.; Abu-Baker, I.; Palmore, G. T. R. Electroreduction of CO2 on Polycrystalline Copper: Effect of Temperature on Product Selectivity. *Catal. Today* **2017**, *288*, 24−29.

(11) Larrazabal, G. O.; Strom-Hansen, P.; Heli, J. P.; Zeiter, K.; Therkildsen, K. T.; Chorkendorff, I.; Seger, B. Analysis of Mass Flows and Membrane Cross-over in CO_2 Reduction at High Current Densities in an MEA-Type Electrolyzer. *ACS Appl. Mater. Interfaces* **2019**, *11* (44), 41281−41288.

(12) Liu, K.; Smith, W. A.; Burdyny, T. Introductory Guide to Assembling and Operating Gas Diffusion Electrodes for Electrochemical CO_2 Reduction. *ACS Energy Lett.* **2019**, *4* (3), 639−643.

(13) Comite, A.; Costa, C.; Demartini, M.; Di Felice, R.; Oliva, M. Exploring CO_2 Capture from Pressurized Industrial Gaseous Effluents in Membrane Contactor-Based Pilot Plant. *Int. J. Greenhouse Gas Control* **2017**, *67*, 60−70.

(14) Ota, M.; Abe, Y.; Watanabe, M.; Smith, R. L.; Inomata, H. Methane Recovery from Methane Hydrate Using Pressurized CO_2. *Fluid Phase Equilib.* **2005**, *228*−*229*, 553−559.

(15) Machado, A. S. R.; Nunes, A. V. M.; da Ponte, M. N. Carbon Dioxide Utilization—Electrochemical Reduction to Fuels and Synthesis of Polycarbonates. *J. Supercrit. Fluid.* **2018**, *134*, 150−156.

(16) IEA. *Energy Technology Perspectives 2020:Special Report on Carbon Capture, Utilisation and Storage*; IEA: Paris, 2020.

(17) Edwards, J. P.; Xu, Y.; Gabardo, C. M.; Dinh, C.-T.; Li, J.; Qi, Z.; Ozden, A.; Sargent, E. H.; Sinton, D. Efficient Electrocatalytic Conversion of Carbon Dioxide in a Low-Resistance Pressurized Alkaline Electrolyzer. *Appl. Energy* **2020**, *261*, 114305.

(18) junge Puring, K.; Evers, O.; Prokein, M.; Siegmund, D.; Scholten, F.; Mölders, N.; Renner, M.; Roldan Cuenya, B.; Petermann, M.; Weidner, E.; Apfel, U.-P. Assessing the Influence of Supercritical Carbon Dioxide on the Electrochemical Reduction to Formic Acid Using Carbon-Supported Copper Catalysts. *ACS Catal.* **2020**, *10* (21), 12783−12789.

(19) Li, J.; Kuang, Y.; Meng, Y.; Tian, X.; Hung, W. H.; Zhang, X.; Li, A.; Xu, M.; Zhou, W.; Ku, C. S.; Chiang, C. Y.; Zhu, G.; Guo, J.; Sun, X.; Dai, H. Electroreduction of CO2 to Formate on a Copper-Based Electrocatalyst at High Pressures with High Energy Conversion Efficiency. *J. Am. Chem. Soc.* **2020**, *142* (16), 7276−7282.

(20) Hara, K.; Tsuneto, A.; Kudo, A.; Sakata, T. Electrochemical Reduction of CO_2 on a Cu Electrode under High Pressure: Factors That Determine the Product Selectivity. *J. Electrochem. Soc.* **1994**, *141* (8), 2097−2103.

(21) Bevilacqua, M.; Filippi, J.; Miller, H. A.; Vizza, F. Recent Technological Progress in CO_2 Electroreduction to Fuels and Energy Carriers in Aqueous Environments. *Energy Technol.* **2015**, *3* (3), 197−210.

(22) Huang, L.; Gao, G.; Yang, C.; Li, X.-Y.; Miao, R. K.; Xue, Y.; Xie, K.; Ou, P.; Yavuz, C. T.; Han, Y.; Magnotti, G.; Sinton, D.; Sargent, E. H.; Lu, X. Pressure Dependence in Aqueous-Based Electrochemical CO_2 Reduction. *Nat. Commun.* **2023**, *14* (1), 2958.

(23) Proietto, F.; Schiavo, B.; Galia, A.; Scialdone, O. Electrochemical Conversion of CO_2 to HCOOH at Tin Cathode in a Pressurized Undivided Filter-Press Cell. *Electrochim. Acta* **2018**, *277*, 30−40.

(24) Dufek, E. J.; Lister, T. E.; Stone, S. G.; McIlwain, M. E. Operation of a Pressurized System for Continuous Reduction of CO_2. *J. Electrochem. Soc.* **2012**, *159* (9), F514−F517.

(25) Oppel, N.; Röse, P.; Heuser, S.; Prokein, M.; Apfel, U.-P.; Krewer, U. Unveiling the Kinetics of CO_2 Reduction in Aprotic Electrolyte: The Critical Role of Adsorption. *Electrochim. Acta* **2024**, *490*, 144270.

(26) Zhao, X.; Liu, Y. Unveiling the Active Structure of Single Nickel Atom Catalysis: Critical Roles of Charge Capacity and Hydrogen Bonding. *J. Am. Chem. Soc.* **2020**, *142* (12), 5773−5777.

(27) Morrison, A. R. T.; van Beusekom, V.; Ramdin, M.; van den Broeke, L. J. P.; Vlugt, T. J. H.; de Jong, W. Modeling the Electrochemical Conversion of Carbon Dioxide to Formic Acid or Formate at Elevated Pressures. *J. Electrochem. Soc.* **2019**, *166* (4), E77−E86.

(28) Heuser, S.; Hoof, L.; Pellumbi, K.; Oberndorf, J. N.; Krämer, L.; Blaudszun, D.; Puring, K. J.; Prokein, M.; Mölders, N.; Kilzer, A.; Petermann, M.; Apfel, U.-P. Differential Pressure CO2 Electrolysis Opens the Way for Direct Coupling to Industrial Processes. *Chem Catal.* **2025**, 101393.

(29) Li, J.; Kuang, Y.; Zhang, X.; Hung, W.-H.; Chiang, C.-Y.; Zhu, G.; Chen, G.; Wang, F.; Liang, P.; Dai, H. Electrochemical Acetate Production from High-Pressure Gaseous and Liquid CO_2. *Nat. Catal.* **2023**, *6* (12), 1151−1163.

(30) Qiu, R.; JiaPeng, J. L.; Li, R.; Yan, S.; Li, J.; Zhang, J.; Sun, D. T.; Lan, Z.; Xue, T.; Xu, G.; Cui, L.; Lv, Z.; Li, C.; Hong, Y.; Guo, Y.; Ren, B.; Yang, S.; Li, J.; Han, B. Enhanced Electroreduction of CO_2 to Ethanol via Enriched Intermediates under High CO_2 Pressure. *Green Chem.* **2023**, *25* (2), 684−691.

(31) Liang, S.; Altaf, N.; Huang, L.; Gao, Y.; Wang, Q. Electrolytic Cell Design for Electrochemical CO2 Reduction. *J. CO_2 Util.* **2020**, *35*, 90−105.

(32) Wu, D.; Jiao, F.; Lu, Q. Progress and Understanding of CO_2/CO Electroreduction in Flow Electrolyzers. *ACS Catal.* **2022**, *12* (20), 12993−13020.

(33) Gao, D.; Wei, P.; Li, H.; Lin, L.; Wang, G.; Bao, X. Designing Electrolyzers for Electrocatalytic CO_2 Reduction. *Acta Phys. -Chim. Sin.* **2020**, *37* (5), 2009021.

(34) Higgins, D.; Hahn, C.; Xiang, C.; Jaramillo, T. F.; Weber, A. Z. Gas-Diffusion Electrodes for Carbon Dioxide Reduction: A New Paradigm. *ACS Energy Lett.* **2019**, *4* (1), 317−324.

(35) Burdyny, T.; Smith, W. A. CO_2 Reduction on Gas-Diffusion Electrodes and Why Catalytic Performance Must Be Assessed at Commercially-Relevant Conditions. *Energy Environ. Sci.* **2019**, *12* (5), 1442−1453.

(36) Hara, K.; Sakata, T. Electrocatalytic Formation of CH 4 from CO_2 on a Pt Gas Diffusion Electrode. *J. Electrochem. Soc.* **1997**, *144* (2), 539.

(37) Hara, K.; Sakata, T. Large Current Density CO_2 Reduction under High Pressure Using Gas Diffusion Electrodes. *Bull. Chem. Soc. Jpn.* **1997**, *70* (3), 571−576.

(38) Sodeifian, G.; Usefi, M. M. B. Solubility, Extraction, and Nanoparticles Production in Supercritical Carbon Dioxide: A Mini-Review. *ChemBioEng. Rev.* **2023**, *10* (2), 133−166.

(39) Endrődi, B.; Kecsenovity, E.; Samu, A.; Halmágyi, T.; Rojas-Carbonell, S.; Wang, L.; Yan, Y.; Janáky, C. High Carbonate Ion Conductance of a Robust PiperION Membrane Allows Industrial Current Density and Conversion in a Zero-Gap Carbon Dioxide Electrolyzer Cell. *Energy Environ. Sci.* **2020**, *13* (11), 4098−4105.

(40) Endrődi, B.; Kecsenovity, E.; Samu, A.; Darvas, F.; Jones, R. V.; Török, V.; Danyi, A.; Janáky, C. Multilayer Electrolyzer Stack Converts Carbon Dioxide to Gas Products at High Pressure with High Efficiency. *ACS Energy Lett.* **2019**, *4* (7), 1770−1777.

(41) Li, H.; Li, H.; Wei, P.; Wang, Y.; Zang, Y.; Gao, D.; Wang, G.; Bao, X. Tailoring Acidic Microenvironments for Carbon-Efficient CO_2 Electrolysis over a Ni−N−C Catalyst in a Membrane Electrode Assembly Electrolyzer. *Energy Environ. Sci.* **2023**, *16* (4), 1502−1510.

(42) Cabeza, L. F.; de Gracia, A.; Fernández, A. I.; Farid, M. M. Supercritical CO_2 as Heat Transfer Fluid: A Review. *Appl. Therm. Eng.* **2017**, *125*, 799−810.

(43) Abbott, A. P.; Eardley, C. A. Electrochemical Reduction of CO_2 in a Mixed Supercritical Fluid. *J. Phys. Chem. B* **2000**, *104*, 775−779.

(44) Heßelmann, M.; Bräsel, B. C.; Keller, R. G.; Wessling, M. Simulation-Based Guidance for Improving CO_2 Reduction on Silver Gas Diffusion Electrodes. *Electrochem. Sci. Adv.* **2023**, *3* (1), 2100160.

(45) Bohra, D.; Chaudhry, J. H.; Burdyny, T.; Pidko, E. A.; Smith, W. A. Mass Transport in Catalytic Pores of GDE-Based CO_2 Electroreduction Systems. *ChemRxiv* **2020**.

(46) Long, Z.; Yu, C.; Cao, M.; Ma, J.; Jiang, L. Bioinspired Gas Manipulation for Regulating Multiphase Interactions in Electrochemistry. *Adv. Mater.* **2024**, *36* (21), 2312179.

(47) Hoof, L.; Thissen, N.; Pellumbi, K.; junge Puring, K.; Siegmund, D.; Mechler, A. K.; Apfel, U.-P. Hidden Parameters for Electrochemical Carbon Dioxide Reduction in Zero-Gap Electrolyzers. *Cell Rep. Phys. Sci.* **2022**, *3* (4), 100825.

(48) Melchaeva, O.; Voyame, P.; Bassetto, V. C.; Prokein, M.; Renner, M.; Weidner, E.; Petermann, M.; Battistel, A. Electrochemical Reduction of Protic Supercritical CO_2 on Copper Electrodes. *ChemSusChem* **2017**, *10* (18), 3660−3670.

(49) Pan, B.; Fan, J.; Zhang, J.; Luo, Y.; Shen, C.; Wang, C.; Wang, Y.; Li, Y. Close to 90% Single-Pass Conversion Efficiency for CO_2 Electroreduction in an Acid-Fed Membrane Electrode Assembly. *ACS Energy Lett.* **2022**, *7* (12), 4224−4231.

(50) She, X.; Zhang, T.; Li, Z.; Li, H.; Xu, H.; Wu, J. Tandem Electrodes for Carbon Dioxide Reduction into C_{2+} Products at Simultaneously High Production Efficiency and Rate. *Cell Rep. Phys. Sci.* **2020**, *1* (4), 100051.

(51) Sun, R.; Zhao, J.; Liu, H.; Xue, Y.; Lu, X. Pressure Regulated CO_2 Electrolysis on Two-Dimensional Bi_2O_2Se. *Chem. Commun.* **2025**, *61* (10), 2071−2074.

(52) Chandesris, M.; Médeau, V.; Guillet, N.; Chelghoum, S.; Thoby, D.; Fouda-Onana, F. Membrane Degradation in PEM Water Electrolyzer: Numerical Modeling and Experimental Evidence of the Influence of Temperature and Current Density. *Int. J. Hydrog. Energy* **2015**, *40* (3), 1353−1366.

(53) Collier, A.; Wang, H.; Zi Yuan, X.; Zhang, J.; Wilkinson, D. P. Degradation of Polymer Electrolyte Membranes. *Int. J. Hydrog. Energy* **2006**, *31* (13), 1838−1854.

(54) Sassenburg, M.; Kelly, M.; Subramanian, S.; Smith, W. A.; Burdyny, T. Zero-Gap Electrochemical CO_2 Reduction Cells: Challenges and Operational Strategies for Prevention of Salt Precipitation. *ACS Energy Lett.* **2023**, *8* (1), 321−331.

(55) Reverchon, E.; De Marco, I. Mechanisms Controlling Supercritical Antisolvent Precipitate Morphology. *J. Chem. Eng.* **2011**, *169* (1−3), 358−370.

(56) He, D.; Jiang, P.; Xu, R. Pore-Scale Experimental Investigation of the Effect of Supercritical CO_2 Injection Rate and Surface Wettability on Salt Precipitation. *Environ. Sci. Technol.* **2019**, *53* (24), 14744−14751.

(57) Suekane, T.; Soukawa, S.; Iwatani, S.; Tsushima, S.; Hirai, S. Behavior of Supercritical CO_2 Injected into Porous Media Containing Water. *Energy* **2005**, *30* (11−12), 2370−2382.

(58) Hu, R.; Wan, J.; Kim, Y.; Tokunaga, T. K. Wettability Impact on Supercritical CO_2 Capillary Trapping: Pore-scale Visualization and Quantification. *Water Resour. Res.* **2017**, *53* (8), 6377−6394.

(59) Garg, S.; Xu, Q.; Moss, A. B.; Mirolo, M.; Deng, W.; Chorkendorff, I.; Drnec, J.; Seger, B. How Alkali Cations Affect Salt Precipitation and CO_2 Electrolysis Performance in Membrane Electrode Assembly Electrolyzers. *Energy Environ. Sci.* **2023**, *16* (4), 1631−1643.

(60) Moss, A. B.; Garg, S.; Mirolo, M.; Giron Rodriguez, C. A.; Ilvonen, R.; Chorkendorff, I.; Drnec, J.; Seger, B. In Operando Investigations of Oscillatory Water and Carbonate Effects in MEA-Based CO_2 Electrolysis Devices. *Joule* **2023**, *7* (2), 350−365.

(61) Domingo, C.; Loste, E.; Gómez-Morales, J.; García-Carmona, J.; Fraile, J. Calcite Precipitation by a High-Pressure CO_2 Carbonation Route. *J. Supercrit. Fluid* **2006**, *36* (3), 202−215.